scientific reports

OPEN

Assessment of pulse wave velocity through weighted visibility graph metrics from photoplethysmographic signals

Juan M. Vargas[1], Mohamed A. Bahloul[2], Mohamed M. Boularas[3], Kaan Yuceel[4], Slaheddine Aridhi[4] & Taous-Meriem Laleg-Kirati[1]✉

Pulse Wave Velocity (PWV) is a widely recognized non-invasive biomarker of arterial stiffness and an independent predictor of cardiovascular risk, including atherosclerosis, hypertension, and vascular aging. Accurate, accessible estimation of PWV is, therefore, critical for early cardiovascular health detection and monitoring. This study proposes a novel data-driven approach for PWV estimation using features derived from Limited Penetrable Weighted Visibility Graphs (LPWVGs) constructed from photoplethysmography (PPG) waveforms and their first and second derivatives. By generating multiple LPWVGs with diverse weighting strategies, we capture the PPG signal's rich temporal and morphological characteristics. A wide range of features was extracted, including descriptors from two-dimensional Semi-Classical Signal Analysis (SCSA), frequency-domain features, and morphological shape and local variation metrics. These were used to train an Explainable Boosting Machine (EBM), a glass-box machine learning model combining strong predictive power and interpretability. The proposed method was evaluated using positive and negative testing on real multicycle PPG datasets. The results demonstrate high accuracy and robustness, obtaining an $R^2 = 0.91$ and $RMSE = 0.34$ in the positive test and a $RMSE = 1.49$ for the negative test. These results support the feasibility of this approach for non-invasive PWV estimation in clinical and ambulatory settings, with potential applications in cardiovascular disease screening, risk stratification, and aging research.

Cardiovascular disease (CVD) is the leading cause of death globally[1], with hypertension being a major modifiable risk factor that contributes to cardiovascular and renal complications. Globally, approximately 33% of adults aged 30-79 years are affected by hypertension, defined as systolic blood pressure (SBP) ≥140 mmHg or diastolic blood pressure (DBP) ≥90 mmHg, or the use of antihypertensive medications. Alarmingly, elevated SBP levels, even starting at 110–115 mmHg, are associated with increased risk of cardiovascular morbidity and mortality. High SBP was identified as the leading global risk factor for mortality in 2019, with an estimated 10.8 million deaths (19%) potentially preventable through adequate blood pressure control[2,3]. With advancing age, structural and functional changes in the vasculature, collectively referred to as vascular aging, lead to increased arterial stiffness (AS), which plays a central role in the pathophysiology of isolated systolic hypertension and elevated pulse pressure[4,5].

Among the available biomarkers, arterial stiffness has gained prominence over the past two decades as one of the most powerful and independent predictors of cardiovascular risk[6]. In particular, carotid-femoral Pulse Wave Velocity (cf-PWV) is recognized as the clinical gold standard for non-invasive assessment of AS, with robust evidence linking elevated cf-PWV to all-cause and cardiovascular mortality[7–10]. PWV is defined as the speed at which the pressure wave propagates along the arterial tree and is typically calculated by dividing the distance between two arterial sites by the time the wave takes to travel that distance[11–13]. However, its measurement remains technically challenging and susceptible to operator-dependent errors, limiting its routine application in clinical settings[14]. The accuracy of traditional measurement approaches largely depends on the training and proficiency of healthcare professionals[15].

To overcome these limitations and improve measurement accuracy, different solutions have been studied to improve the estimation of PWV. For example, in 2022, Xu et al.[16] proposed to estimate Carotid-femoral PWV based on a simplified tude-load model that allows a model of the propagation and the reflection of the pulse wave.

[1]Université Paris-Saclay, Inria, CIAMS, Gif-sur-Yvette 91190, France. [2]College of Engineering & Advanced Computing, Alfaisal University, Riyadh 11533, Saudi Arabia. [3]Sorbonne Université, Paris 75005, France. [4]Sensoria Analytics, Valbonne 06560, France. ✉email: taous-meriem.laleg@inria.fr

In 2023, Park et al.[17] proposed the estimation of aortic PWV using 4D flow MRI images and a cross-correlation algorithm, allowing regional PWV estimation. In addition, in 2024, Yang et al.[14] used a semi-automatic Doppler ultrasound-based method for regional Carotid-femoral and Femoral-ankle PWV estimation. Recently, data-driven approaches leveraging photoplethysmography (PPG) signals have gained increasing attention. The main advantage of PPG-based methods lies in their non-invasive and easy-to-implement nature, which addresses several key drawbacks of conventional techniques. Traditional PWV estimation requires the simultaneous acquisition of pulse wave signals from two arterial sites — a technically complex, operator-dependent, and often invasive procedure.

In contrast, PPG-based methods enable single-site signal acquisition, significantly reducing setup complexity and operator dependency. Moreover, the ability to record PPG signals non-invasively and with minimal effort opens the door to routine clinical use and continuous monitoring through wearable devices such as smartwatches and fitness trackers[18]. For example, Bahloul et al.[19] introduced a machine learning-based method using a multilayer perceptron trained on features extracted from the PPG waveform and its derivatives to estimate Pulse Wave Velocity (PWV). Another study by Weiwei et al. cites Jin proposed two machine learning pipelines—Gaussian Process Regression and Recurrent Neural Networks—to estimate carotid-femoral PWV (cf-PWV) from radial blood pressure waveforms measured via applanation tonometry.

Following these developments, Vargas et al.[20] investigated Semi-Classical Signal Analysis (SCSA) features derived from both blood pressure (BP) and PPG signals, using a linear regression model to predict PWV, explicitly focusing on measurements from the carotid to femoral arteries. In a separate study, Vargas et al.[21] proposed a novel approach by transforming PPG signals into spectrogram images and extracting image-based features for PWV estimation. Their results underscored the potential of signal-to-image transformation in this domain.

Additionally, Vargas et al.[22] introduced a binary visibility graph approach using the binary adjacency matrix within a transfer learning framework for PWV estimation. Hellqvist et al.[23] proposed a set of novel fiducial-point-based features, which were then used as inputs to LASSO and Random Forest models for the estimation of cf-PWV and aortic PWV (aoPWV).

More recently, Pilevar et al.[24] extended the signal-to-image paradigm by employing a deep learning architecture based on convolutional neural networks (CNNs) and attention mechanisms to estimate PWV from spectrogram images. Debuchy et al.[25] proposed combining PPG signals acquired from different body sites and extracted features based on fiducial points from the PPG and its derivatives.

Finally, Vargas et al.[26] introduced a novel method combining visibility graphs (VG) and image processing techniques applied to both in-silico and real datasets. However, due to the scarcity of high-quality, real-world data, many of these studies relied on single-cycle in-silico PPG datasets, which may limit the generalizability of their findings.

In this study, we propose a comprehensive framework for PWV estimation based on multicycle PPG signals and their first and second derivatives, which provide insights into signal velocity and acceleration. This approach leverages the physical interpretation of the PPG derivatives, which carry valuable information related to PWV[19], and combines it with the representational power of the Limited Penetrable Weighted Visibility Graph (LPWVG) adjacency matrix offering a rich representation of the inner dynamics of the PPG and effectively capturing the intrinsic behavior associated with PWV.

Additionally, we employ glass-box models, such as the Explainable Boosting Machine (EBM), which enhance interpretability and support robust model evaluation. Using positive and negative testing further strengthens the assessment of model performance in realistic scenarios. We compare our results with several state-of-the-art PPG-based methods for PWV estimation, demonstrating our approach's effectiveness and clinical relevance.

Methodology

Figure 1 illustrates the pipeline proposed for PWV estimation. First, the signal is obtained from the radial artery, and its first and second derivatives are computed. Next, the original signal and its derivatives are transformed into images using a visibility graph with the proposed weighting schemes. Finally, for each image, three features—based on shape, texture, and energy—are extracted and fed into an Explainable Boosting Machine (EBM) to estimate the PWV.

Dataset

The proposed methodology is validated using simulated in-silico signals and real PPG multicycle signals to assess the performance under various scenarios.

Real PPG dataset
The real-world dataset includes pulse wave velocity (PWV) measurements, which serve as indicators of central artery stiffness, along with pulse wave recordings for the PWV was acquired using the SphygmoCor device. The associated PPG signals were recorded at the finger with a sampling frequency of 200 Hz for 5 minutes per patient to ensure minimal discomfort. The PPG signal acquisition was done using the BM3000B oximeter and the cardioSensys acquisition SW. This PPG signal is obtained from the infrared LED operating at 940 nm. The dataset consists of recordings from 35 subjects aged between 35 and 73.

In-silico dataset
Due to the lack of real hemodynamic data for validating and testing PWV estimation frameworks, previous studies[21,24,25] have relied on a public in-silico hemodynamic database to evaluate the performance of their methods (https://peterhcharlton.github.io/pwdb/index.html). This dataset was generated using a one-dimensional model
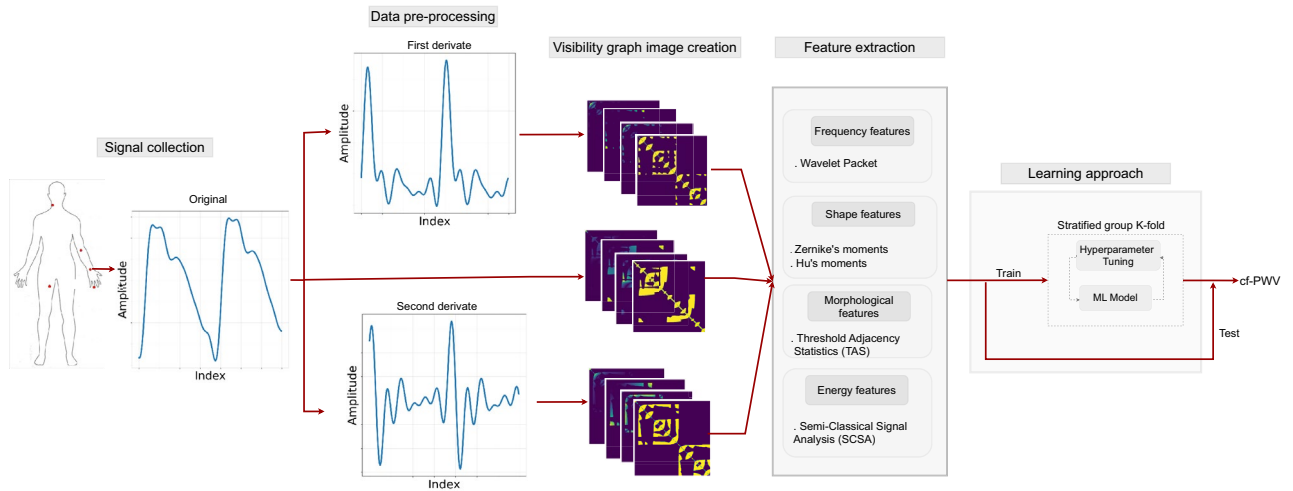
Fig. 1. Pulse wave velocity estimation based on Limit Penetrable Weighted Visibility Graph (LPWVG) and image processing feature extraction wave images. The proposed framework takes the signal obtained from the radial artery and computes the first two derivatives. Then, the three signals are transformed into images using a visibility graph and the different weights proposed. Finally, for each image, a set of three different types of features based on shape, texture, and energy are extracted and fed into an EBM (Explainable Boosting Machine) to estimate the PWV.

that simulates pulse wave signals at various arterial locations. The model accounts for different cardiovascular properties such as age, heart rate, blood density, and arterial diameter, among other parameters[27].

The database includes 4,374 virtual healthy adults, aged between 25 and 75 years, grouped into six 10-year age intervals. Heart rates range from 66 to 86 bpm, and all signals were generated at a sampling frequency of 500 Hz. Each age group comprises 729 virtual subjects with distinct cardiac and arterial characteristics, including arterial stiffness and heart rate variations within normal physiological ranges.

In this study, PPG waveforms from the radial artery were used to construct visibility graphs and estimate PWV.

Data pre-processing
Data filtering
A data filtering method has been implemented to enhance the quality of PPG signals. Recent research[28] has indicated that employing an 18th-order pass-band Chebyshev II filter with a low-cut frequency of 0.5 Hz and a high-cut frequency of 10 Hz ensures the preservation of the physiological information carried by the signals. Additionally, for each subject, we selected the best 30-second segment of the recording where the signal exhibited no apparent noise or abnormal behavior such as motion artifacts. From this segment, we generated 10 nonoverlapping windows of 3 seconds in length. Features were extracted from each window individually, and the median value across all windows for each feature was computed. This approach provided a robust and representative feature vector per subject, minimizing the influence of transient noise or outliers in the signals.

Derivatives computation
After filtering the data, the first and second derivatives of the PPG signal (PPG' and PPG'') were computed as shown in Fig. 2. This preprocessing step is inspired by previous studies[19,25], highlighting the importance of PPG derivatives for extracting key information related to the velocity and acceleration of the underlying physiological processes. Incorporating these derivatives has enhanced model performance by capturing more complex information about the blood flow behavior shown by the PPG signal.

Visibility graph method
To transform PPG waveforms into images, we propose using a technique called the Visibility Graph (VG). This method converts time series into networks, capturing the underlying dynamics of the signal in the resulting network topology. The core idea of the VG representation is to treat each data point in the original signal as a node. Edges are then established between nodes based on a visibility criterion applied to the signal[29,30].

Let $y = [y1, \cdots, y_T]$ represent a time series of T points, two points (t_a, y_a) and (t_b, y_b) are considered naturally visible to each other if every intermediate point (t_c, y_c), such that $t_a < t_c < t_b$, satisfies the following visibility criteria if: (Eq. 1 and Fig.3).

$$y_c < y_a + (y_b - y_a)\frac{t_c - t_a}{t_b - t_a}, \tag{1}$$

i.e., we can draw a straight line between them without any intersection.
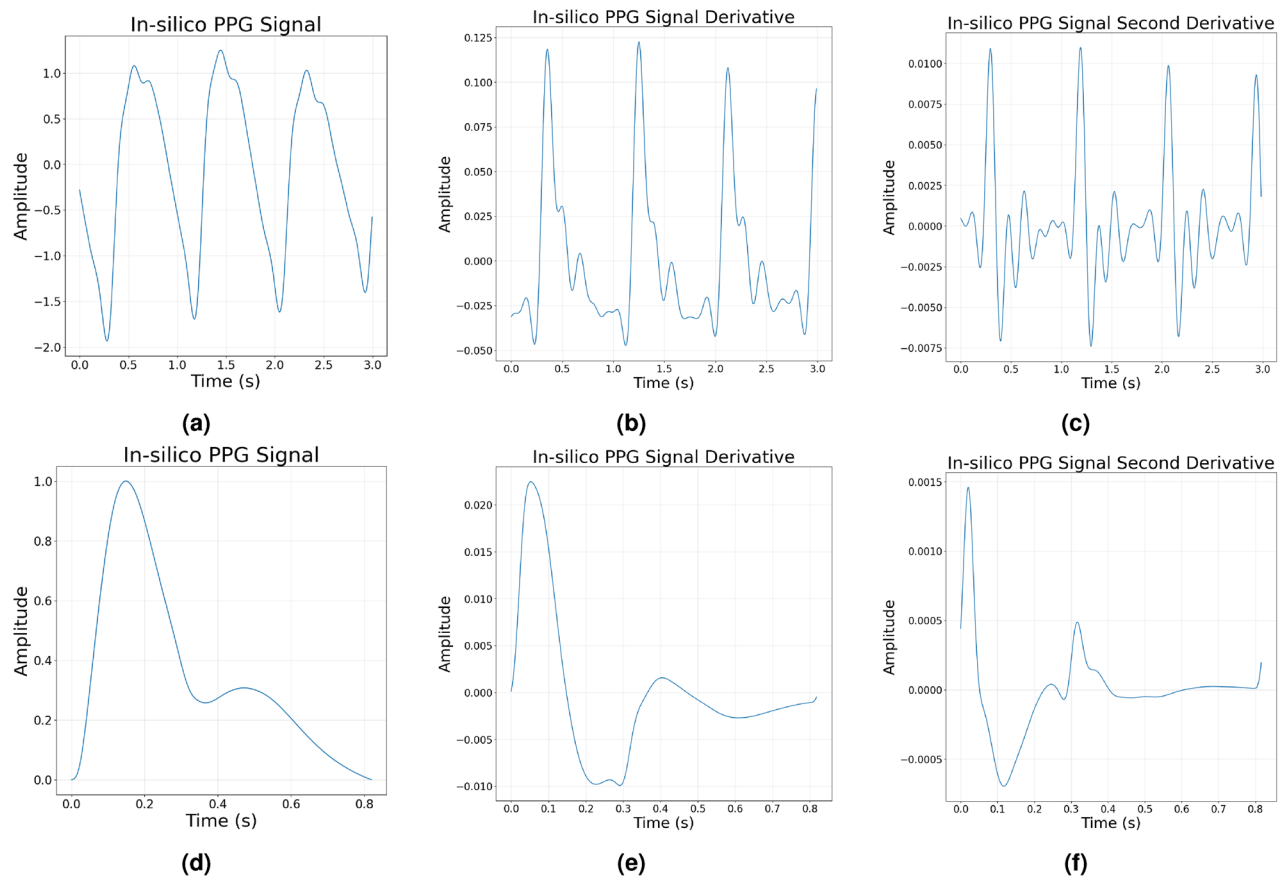
Fig. 2. Comparison of photoplethysmography (PPG) signals and their derivatives from real and in-silico datasets. (**a**–**c**) Multicycle real PPG signal and its first and second derivatives, showing natural variability and noise representative of physiological conditions. (**d**–**f**) In-silico PPG signal and its derivatives exhibiting smoother and idealized waveform characteristics. The first derivatives emphasize the rate of change in signal amplitude, while the second derivatives highlight inflection points and subtle waveform features. While in-silico signals are valuable for controlled modeling and initial algorithm development, the real PPG data are essential for evaluating performance under realistic conditions, capturing inter-cycle variability, and biological noise important for robust and clinically relevant analysis.

Remark An undirected and unweighted graph is constructed from the signal, where each node represents a data point, and edges indicate the visibility between pairs of nodes.

Signal to image transformation
As mentioned above, this project explores a novel signal-to-image transformation based on the visibility graph for PWV estimation. The transformation involves constructing an adjacency matrix A of size $T \times T$, where T is the length of the PPG signal. In this representation, $A_{i,j} = 1$ if the points (t_a, y_a) and (t_b, y_b) are visible to each other according to the visibility criterion, and $A_{i,j} = 0$ otherwise (Fig. 3).

Figure 4 illustrates the process of generating images based on the visibility criterion in greater detail. As shown, the edges near the image's corners represent long-term relationships between points in the signal. In the context of this project, such relationships allow us to analyze interactions between different PPG cycles—a valuable advantage, as multicycle dynamics have been shown to play an essential role in vascular compliance. In contrast, points near the diagonal capture short-term relationships, reflecting rapid events within a single cardiac cycle. This makes the visibility graph a powerful representation for converting signals into images. Consequently, extracting image-based features that capture key aspects such as shape, texture, and energy comprehensively describe the underlying dynamics in the PPG recording.

Permeability parameter selection
One of the key strengths of visibility graphs is their inherent ability to provide a robust representation of the signal, even in the presence of noise[31]. This robustness is achieved through a permeability parameter (p), which allows two nodes in the graph to be connected even if one or more data points lie between them.

The value of p defines the number of intermediate data points that can be ignored when evaluating the visibility between two nodes. When $p = 0$, the traditional visibility graph is obtained, where no intermediate points are allowed. Higher values of p enable the graph to overlook one or more intermediate points—potentially
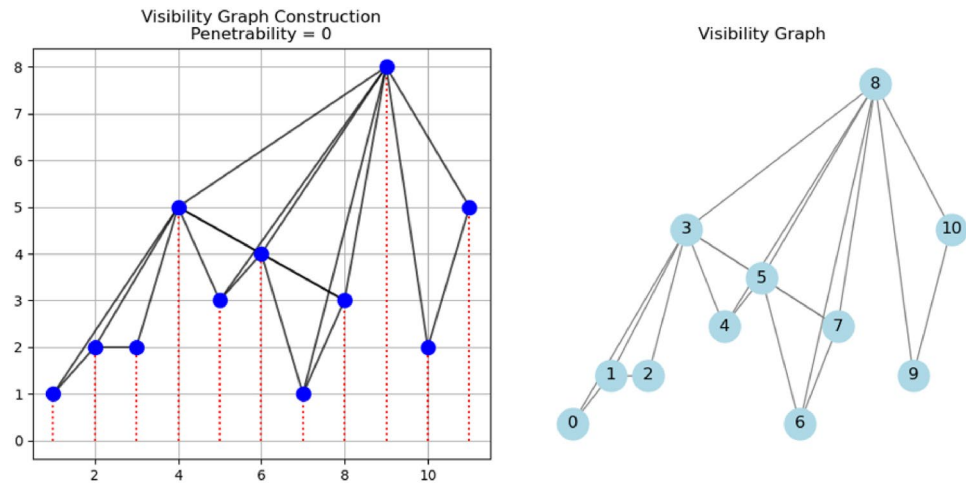
Fig. 3. Visibility graph construction using the natural visibility criteria. The left panel illustrates the transformation of a time series into a graph by connecting data points (nodes) with straight lines when no intermediate point obstructs the line of sight — a condition defined by zero penetrability. The resulting graph structure is shown in the right panel, where nodes represent time series points, and edges indicate visibility connections. This technique enables the mapping of temporal dynamics into complex network structures, allowing time-series analysis through graph-theoretical metrics and providing insights into the signal's structure, periodicity, and hidden patterns.
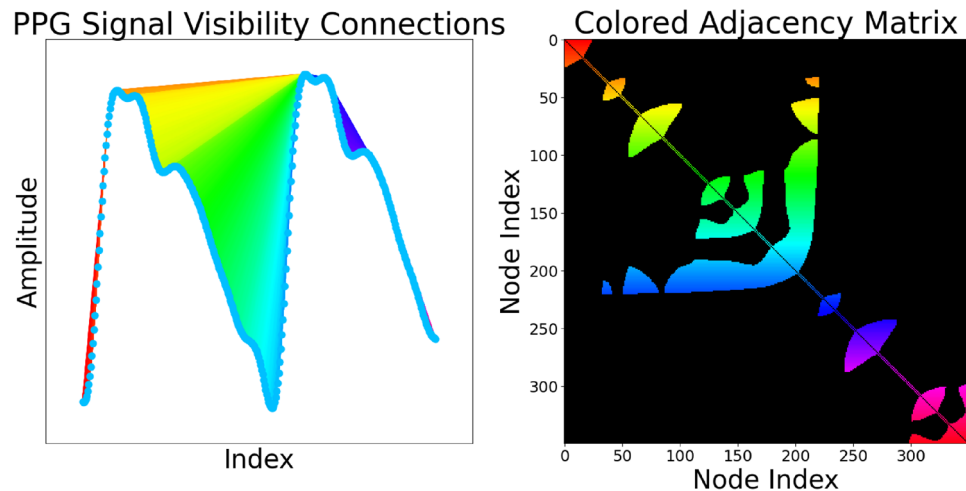

Fig. 4. Signal-to-image transformation using a visibility graph approach. (Left) A photoplethysmography (PPG) signal is visualized with visibility connections drawn between data points that satisfy the natural visibility criteria. (Right) The corresponding colored adjacency matrix encodes these connections, where each color represents different visibility relationships among nodes (signal points). This transformation enables the conversion of temporal signal characteristics into a structured image format, facilitating subsequent analysis using image-based or deep-learning methods.

caused by noise—thus preserving meaningful connections. However, it is essential to note that increasing p may also introduce additional connections in regions where none previously existed, potentially altering the graph's structure.

In addition, as discussed in[32], higher values of p improve the ability of the VG to capture long-term relationships between the different points of The PPG allows for capturing the relationship between cycles, increasing the amount of information the graph captures.

Weighting selection
However, for certain types of applications, it has been shown that assigning different weights to the edges can enhance the graph representation (Fig. 5), allowing a more precise capture of the relationships between the values of a signal. While unweighted graphs capture only the presence or absence of visibility between signal points, giving the same value to each connection, weighted visibility graphs incorporate quantitative information about
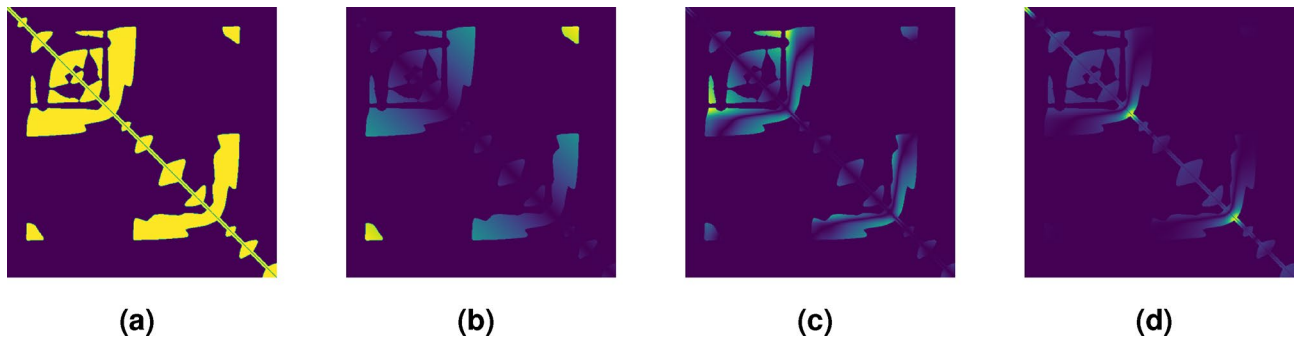
Fig. 5. Different weights for the visibility graph's adjacent matrix representation of the multicycle PPG signal. (**a**) Unweighted. (**b**) Horizontal distance. (**c**) Vertical distance. (**d**) Absolute angle of view. This image represents some examples of the weights used in the project; as we can see, the image obtained is no longer binary, as in the case of (**a**). In addition, each different weight type will focus on different characteristics from the visibility graph, such as time relationships or intensity differences between points. This new information will help extract richer information from the underlying dynamics of the PPG signals.

the strength or nature of these connections, giving different numerical values to the connections. This allowed for improving the capacity of the visibility graph representation to capture subtle changes in the PPG waveform intensity and time evolution that can improve the pulse wave velocity estimation. In this project, multiple visibility graph representations were computed for each PPG signal and its derivatives using the following weights (as can be seen in the Fig. 1):

- Euclidean distance: This metric defines the weight of the edges based on the Euler distances between the two visible points. This weight has the characteristics of incorporating both time and intensity differences between the two points. This allows us to capture more complete information about the morphology of the signal.

$$ECw_{i,j} = \sqrt{(y_b - y_a)^2 + (t_b - t_a)^2}. \tag{2}$$

- Square Euclidean distance: This metric defines the weight of the edges based on the square Euler distances between the two visible points. Similarly to the Euclidean distance, this weight combines the distance information in time and intensity. However, in this case, more considerable distances are emphasized compared to the regular Euclidean metric, making distant points contribute more heavily. This allows us to understand how distant points interact with each other.

$$SECw_{i,j} = (y_b - y_a)^2 + (t_b - t_a)^2. \tag{3}$$

- Vertical distance and absolute vertical distance: These metrics define the weight of the edges based on the intensity difference (Vw) and the absolute intensity difference (AVw) between the two visible points. These weights capture variations in the intensities, giving information about the topological structure of the signal. The main difference between the two metrics is that while Vw differentiates if the points are higher or lower than the point studied, AVw threatens the upward and downward movement equally.

$$Vw_{i,j} = y_b - y_a. \tag{4}$$

$$AVw_{i,j} = |y_b - y_a|. \tag{5}$$

- Horizontal distance and absolute horizontal distance: These metrics define the weight of the edges based on the time difference (Hw) and the absolute intensity difference (AHw) between the two visible points. For this reason, these weights capture the time relation between the points, giving more weight to the more significant time difference between the two visible points. This plays an essential role in studying the causality and dynamic evolution of the signal. The weights Hw allow us to examine how different points in the past affect the current point and how the current point will affect the future evolution of the signal. In contrast, AHw captures the sparsity in time of the signal by removing the directional influence, treating forward and backward time steps the same.

$$Hw_{i,j} = t_b - t_a. \tag{6}$$

$$AH_{i,j} = |t_b - t_a|. \tag{7}$$

- Slope and absolute slope: This metric defines the weight of the edges based on the slope (Sw) and the absolute slope (ASw) between the two visible points. In other words, these weights represent the rate of change between two visible points, capturing steepness and direction. These characteristics give a strong representation of the trend and the morphology of the signal, where, in the case of Sw, the direction of the change is captured. At the same time, for ASw, there is no difference in the direction of the change, only focusing on the amount of change.

$$Sw_{i,j} = \frac{y_b - y_a}{t_b - t_a}. \tag{8}$$

$$ASw_{i,j} = \left| \frac{y_b - y_a}{t_b - t_a} \right|. \tag{9}$$

Feature extraction

The feature extraction process applied in this project (Fig. 1) involved computing four types of features (frequency, shape, morphological, and energy) across all visibility graph representations generated using the various weighting strategies described in Section "Weighting selection". After feature computation, all features extracted from each weighted graph are concatenated, representing different independent features. This approach gives as results a rich, multi-perspective representation of each signal, where the contribution of each weighting strategy helps to enhance the capacity to estimate the Pulse Wave Velocity.

Shape-based features:
Hu's moments and Zernike's moments are known features in image processing that describe the shape of different objects in an image by defining the pixel distribution of the object within an image. By combining Hu's moments for global shape information and Zernike's moments for localized shape information, this study aims to comprehensively describe the shape of the PPG image representation.

Hu's moments Hu's moments are invariant moments that capture an object's global shape and morphology characteristics[33]. They have been widely used for shape recognition and object matching, demonstrating remarkable robustness against translation, rotation, and scale variations[34,35]. These moments are composed of 7 orthogonal moment invariants that are described as follows:

$$I_1 = \eta_{20} + \eta_{02} \tag{10}$$

$$I_2 = (\eta_{20} - \eta_{02})^2 + 4\eta_{11}^2 \tag{11}$$

$$I_3 = (\eta_{30} - 3\eta_{12})^2 + (3\eta_{21} - \eta_{03})^2 \tag{12}$$

$$I_4 = (\eta_{30} + \eta_{12})^2 + (\eta_{21} + \eta_{03})^2 \tag{13}$$

$$I_5 = (\eta_{30} - 3\eta_{12})(\eta_{30} + \eta_{12})[(\eta_{30} + \eta_{12})^2 \\ - 3(\eta_{21} + \eta_{03})^2] + (3\eta_{21} - \eta_{03})(\eta_{21} + \eta_{03}) \\ [3(\eta_{30} + \eta_{12})^2 - (\eta_{21} + \eta_{03})^2] \tag{14}$$

$$I_6 = (\eta_{20} - \eta_{02})[(\eta_{30} + \eta_{12})^2 - (\eta_{21} + \eta_{03})^2] \\ + 4\eta_{11}(\eta_{30} + \eta_{12})(\eta_{21} + \eta_{03}) \tag{15}$$

$$I_7 = (3\eta_{21} - \eta_{03})(\eta_{30} + \eta_{12})[(\eta_{30} + \eta_{12})^2 \\ - 3(\eta_{21} + \eta_{03})^2] + (\eta_{30} - 3\eta_{12})(\eta_{21} + \eta_{03}) \\ [3(\eta_{30} + \eta_{12})^2 - (\eta_{21} + \eta_{03})^2], \tag{16}$$

where $\eta_p q$ corresponds to the normalized central moments from the image, defined as:

$$\eta_{pq} = \frac{\sum_{x=1}^{M} \sum_{y=1}^{N} (x - \overline{x})^p (y - \overline{y})^q I[x,y]}{\left(\sum_{x=1}^{M} \sum_{y=1}^{N} I[x,y] \right)^\gamma} \tag{17}$$

$$\text{with } \gamma = \frac{p+q}{2} + 1, \quad \forall p + q \geq 2$$

where $p, q = 0, 1, 2, 3, \ldots$, where p, q are non-negative integers and $(p + q)$ is called the order of the moment. $\overline{x}$ and $\overline{y}$ represent the coordinates of the centroid of the image.

Zernike's moments Zernike's moments constitute a set of orthogonal polynomial moments defined over the interior of the unit disc in polar coordinates space, offering a concise representation of an image's shape, robust to different transformations such as the rotation of the objects in the image. These moments excel at capturing local shape information and distinguishing subtle variations in the shapes of an image[33,36]. The Zernike moments for a digital image I are defined as follows:

$$Z_{n,m} = \frac{m+1}{\pi} \sum_{x=1}^{M} \sum_{y=1}^{N} I[x,y]\, V_{n,m}^*(r,\theta) \tag{18}$$

where n is a nonnegative integer related to the order of the momentum and m is the repetition. These two values follow $n - |m|$ is even, and $|m| \leq n$. In addition, $V_{n,m}^*$ is the complex conjugate of Zernike polynomial $V_{n,m}$ defined as :

$$V_{n,m}(r,\theta) = R_{n,m}(r)\, e^{jm\theta} \tag{19}$$

where $R_{n,m}$ is the radial polynomial defined as:

$$R_n^m(r) = \sum_{s=0}^{\frac{n-|m|}{2}} (-1)^s \frac{(n-s)!}{s!\left(\frac{n+|m|}{2} - s\right)!\left(\frac{n-|m|}{2} - s\right)!}\, r^{n-2s} \tag{20}$$

Morphological-shape
In this study, the threshold adjacency statistics (TAS) features proposed by[37] were used for local morphology feature extraction. This method has been used as feature extraction for different image processing applications such as microcalcification detection[38] or breast cancer classification[39]. The main idea of TAS is to threshold an image based on the mean intensity and count the number of white pixels that present the patterns shown in the Fig. 6.

Then, based on this, six different thresholds are used, generating 54 TAS features.

Frequency-based features:
In this study, Wavelet packet features were employed for frequency-based analysis. The 2-D Wavelet Packets (WP) decomposition represents a simple modification of the 2-D Discrete Wavelet Transform (DWT), offering
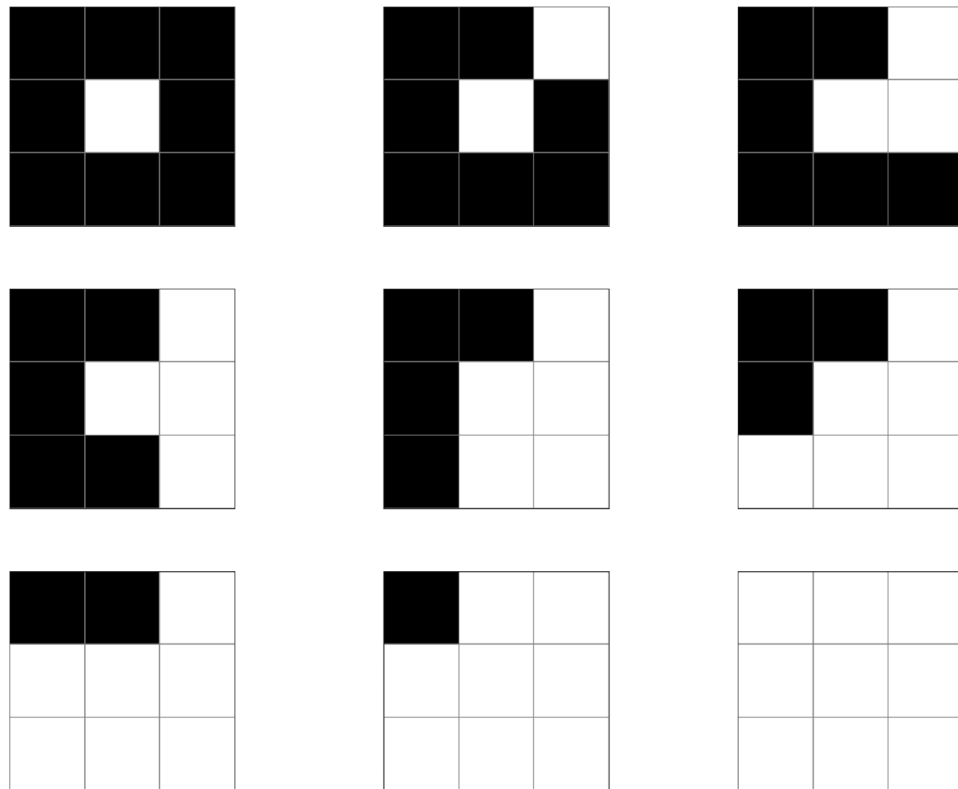
Fig. 6. Representative 3×3 binary pixel patterns used to compute the 9 Texture Analysis Statistical (TAS) features for each threshold level. Each pattern corresponds to a specific spatial configuration of black (foreground) and white (background) pixels within a local neighborhood. These patterns are designed to capture variations in local morphology and structure across the image. They are used as the basis for calculating statistical descriptors that characterize image intensity, uniformity, and contrast under different threshold conditions.

a richer space-frequency representation for image processing[40]. This enhancement arises since each sub-image derived from the standard 2-D DWT is further decomposed into four additional sub-images, known as DWPT coefficients. For example, statistical measures such as the mean and standard deviation of these coefficients provide insights into both the micro-textures (local texture) and macro-textures (global texture) of an image.

At is define in, the 2D-WP of a image I up to level $P + 1$ with $P \leq min(log_2 N, log_2 M)$ as:

$$C^{p+1}_{4k,(i,j)} = \sum_m \sum_n h(m)h(n)C^p_{k,(m+2i,n+2j)} \tag{21}$$

$$C^{p+1}_{4k+1,(i,j)} = \sum_m \sum_n h(m)g(n)C^p_{k,(m+2i,n+2j)} \tag{22}$$

$$C^{p+1}_{4k+2,(i,j)} = \sum_m \sum_n g(m)h(n)C^p_{k,(m+2i,n+2j)} \tag{23}$$

$$C^{p+1}_{4k+3,(i,j)} = \sum_m \sum_n g(m)g(n)C^p_{k,(m+2i,n+2j)} \tag{24}$$

, where C^0_0 is the image I and k, is an index of the nodes in the wavelet packet tree denoting each subband. At each step, the image C^p_k is decomposed into four quarter-size images $C^{p+1}_{4k}, C^{p+1}_{4k+1}, C^{p+1}_{4k+2}, C^{p+1}_{4k+3}$.

These DWPT coefficients allow us to study the image patterns under different resolutions and orientations, providing a robust method to capture macro-texture related to the first levels of the wavelet packet features and micro-textures that the last levels of the wavelet packet features will describe. In this project, three levels of WP features were used to characterize the texture presented by the visibility graph image representation of the PPG signal.

SCSA-based features:
The SCSA (Semi-Classical Signal Analysis) method is a signal processing technique based on the adaptive decomposition of signals into a set of squared eigenfunctions of the Schrödinger operator[41]. This approach has been successfully extended to image processing, showing strong performance as a feature extraction method for PWV estimation[20,21]. The core idea behind the extracted features is to leverage a set of spectral parameters derived from the original signal—specifically, the eigenfunctions and their corresponding eigenvalues obtained from the Schrödinger spectrum, as follows:

Let $I(x, y)$ be a positive real-valued square matrix, the image representation I_{2h} of $I(x, y)$ using the 2D-SCSA is defined as follows:

$$I_{2h}(x, y) = \left[\frac{h^2}{L^{cl}_{2,\gamma}} \sum_{m=1}^{M_h} (-\lambda_{mh})^\gamma \psi^2_{mh}(x, y) \right]^{\frac{1}{\gamma+1}} \tag{25}$$

where $h \in \mathbb{R}^*_+$ is known as the semi-classical signal parameter, $\gamma \in \mathbb{R}_+$ will be used to change the intensity of the pixels during the reconstruction to increase the contrast. $\lambda_{1h}, \lambda_{2h}\cdot, \lambda_{M_h h}$ are the negative eigenvalues, and $\Psi_{1h}, \Psi_{2h}, \ldots, \Psi_{M_h}$ correspond to their associated L^2-normalized eigenfunctions ($m = 1, \ldots, M_h$ the number of eigenvalues) of the two-dimensional semi-classical Schrödinger operator described as follows:

$$H_{2,h}(I)\psi = -h^2 \left(\frac{\partial^2 \psi}{\partial x^2} + \frac{\partial^2 \psi}{\partial y^2} \right) - I\psi \tag{26}$$

and $L^{cl}_{2,\gamma}$ is the suitable semi-classical constant defined as:

$$L^{cl}_{2,\gamma} = \frac{1}{(2\sqrt{\pi})^2} \frac{\Gamma(\gamma + 1)}{\Gamma(\gamma + 2)} \tag{27}$$

where Γ is the Gamma function.

Features extracted for the spectral parameters have proven highly effective in providing valuable insights into the image's energy and global and local morphology. Moreover, one of the key advantages of these features lies in their robustness against noisy data, attributed to the inherent capacity of SCSA to handle such noise[20,42,43]. Specifically, the SCSA features have demonstrated a remarkable ability to capture pertinent information from PPG signals that strongly correlate with PWV values[20,21], underscoring their importance. Therefore, in this study, we propose to extract a predefined set of spectral parameters calculated previously in[20], defined as

$$\text{INV}_1 = 4h \sum_{n=1}^{N_h} \sum_{m=1}^{M_h} \kappa_h[m, n] \tag{28}$$

$$\text{INV}_2 = \frac{16h}{3} \sum_{n=1}^{N_h} \sum_{m=1}^{M_h} \kappa_h[m, n]^3 \tag{29}$$

$$\text{INV}_3 = \frac{256h}{7} \sum_{n=1}^{N_h} \sum_{m=1}^{M_h} \kappa_h[m,n]^7 \tag{30}$$

$$\kappa[m,n]_h = (-\lambda_{mh})^{\gamma} \tag{31}$$

$$\text{K}_n = \frac{1}{M_h} \sum_{m=1}^{M_h} \kappa_h[i,n], \tag{32}$$

$$\text{E}_n = \frac{1}{M_h} \sum_{m=1}^{M_h} (\kappa_h[i,n])^{\frac{1}{\gamma}} \quad n = [1,2,3] \tag{33}$$

$$\text{R}_h = \frac{\kappa_{1h}}{h}, \quad \text{MR}_h = \frac{\text{median}(\kappa_{mh})}{h} \tag{34}$$

Finally, the features used in this project are summarized in Table 1.

Feature selection

Feature selection is a crucial step in machine learning and data analysis, aimed at improving model performance by focusing on the most informative variables, reducing complexity, and enhancing interpretability. In this project, feature selection was performed by identifying the top K features based on their correlation with PWV. Multiple correlation methods—Pearson, Spearman, Kendall, and Xicor—captured various relationships between features and PWV. Each method was used independently to select its top K features, leveraging their respective strengths in identifying linear, monotonic, or nonlinear dependencies.

To ensure diversity and avoid redundancy, any feature that appeared among the top K of more than one method was included only once in the final set. In this project, the top 8 features were selected from each correlation method, resulting in a combined set of 32 unique features, as presented in Table 2.

As can be observed in Table 2, the selected features were grouped based on their origin to better understand their contributions to PWV estimation. The majority of features selected were morphological-based, particularly Threshold Adjacency Statistics (TAS) and Zernike's Moments, reflecting their ability to capture detailed local shape variations and structural characteristics of the PPG waveform. Additionally, several slope and distance-based metrics derived from the original signal and its derivatives underline the significance of waveform derivatives, as these features offer insights into signal velocity and acceleration. Notably, features extracted from second derivatives, such as the absolute slope and vertical distance metrics, emerged frequently, underscoring their crucial role in providing additional physiological insights into vascular stiffness.

Machine learning models

The Explainable Boosting Machine (EBM) model was then employed for predictions. This ML model belongs to the class of glass-box machine learning methods, a subset of ML models based on the Generalized Additive Models (GAMs) family, designed to balance the trade-off between high predictive performance and interpretability. It is an ideal choice for medical applications where understanding the relationship between features and predictions is crucial, as it allows us to be more secure about the findings given by the models[44]. The main idea of this method is to construct interpretable models by combining boosted, shallow decision trees to estimate the contribution of each feature in the prediction and interactions between selected features. This approach enables the model to capture complex, nonlinear relationships while maintaining a structure that allows each feature's contribution to be explicitly visualized and understood. Furthermore, EBM incorporates bagging and boosting techniques to ensure robustness and achieve competitive performance comparable to state-of-the-art black-box models while significantly reducing the risk of overfitting[45].

To validate our choice of EBM, we conducted a comparative evaluation with several other regression models, including both glass-box models—LassoCV, ElasticNetCV, Bayesian Ridge, and Gamma Regressor—and more

Feature Type	Feature Name	Description
Shape-based	Hu's Moments	Global shape features, invariant to translation, rotation, and scale.
	Zernike's Moments	Localized shape features using orthogonal polynomials for fine-grained shape characterization.
Morphological-based	TAS	Local morphological features based on pixel connectivity for local morphology characterization.
Frequency-based	Wavelet Packet Features	Statistical measures (mean, std.) from 2D Wavelet Packet Transform, capturing texture.
SCSA-based	$\text{INV}_1, \text{INV}_2, \text{INV}_3$	Invariants derived from eigenvalues.
	K_n	Average spectral parameter per eigenvalue.
	E_n	Normalized energy from eigenvalues.
	R_h	Ratio of the first eigenvalue to the SCSA parameter h.
	MR_h	Median ratio of eigenvalues scaled by h.

Table 1. Summary of Features Used in the Study.

| Category	Metrics
Morphological-based (TAS features)	first_derivative_abs_slope_TAS22
	second_derivative_abs_slope_TAS51
	second_derivative_abs_slope_TAS21
	second_derivative_abs_slope_TAS37
	first_derivative_slope_TAS7
	first_derivative_slope_TAS16
	first_derivative_v_distance_TAS31
	second_derivative_abs_slope_TAS33
	second_derivative_abs_slope_TAS13
	first_derivative_abs_slope_TAS52
	second_derivative_abs_slope_TAS4
	original_abs_slope_TAS46
	second_derivative_distance_TAS50
	second_derivative_h_distance_TAS50
Shape-based (Zernike's and Hu's moments)	second_derivative_v_distance_Zernikes_Moments_radius_9_13.1
	original_abs_slope_Zernikes_Moments_radius_9_8.1
	original_distance_Zernikes_Moments_radius_9_8.1
	original_h_distance_Zernikes_Moments_radius_9_8.1
	second_derivative_abs_v_distance_Zernikes_Moments_radius_9_10.2
	second_derivative_slope_Zernikes_Moments_radius_9_2
	original_abs_v_distance_Zernikes_Moments_radius_9_11.2
	original_slope_Zernikes_Moments_radius_9_11.1
	first_derivative_abs_slope_Zernikes_Moments_radius_9_5
	first_derivative_distance_Zernikes_Moments_radius_9_5
	first_derivative_abs_v_distance_Zernikes_Moments_radius_9_5
	original_distance_Zernikes_Moments_radius_9_0.2
	original_abs_v_distance_Zernikes_Moments_radius_9_8.1
	original_v_distance_Zernikes_Moments_radius_9_14.1
	second_derivative_v_distance_Hu_Moment_6
SCSA-based	first_derivative_abs_v_distance_K2sq_sum
	first_derivative_abs_slope_INV1_sums

Table 2. Feature selected in this project.

Model	R-squared	RMSE
Explainable Boosting Machine (EBM)	0.91	0.16
LassoCV	0.61	0.58
ElasticNetCV	0.68	0.52
Bayesian Ridge	0.76	0.45
Gamma Regressor	0.76	0.45
Random Forest	0.37	0.73
Gradient Boosting	0.01	0.92
Support Vector Regressor (SVR)	0.11	0.87

Table 3. Comparison of model performance on the test dataset using R-squared and RMSE.

complex black-box models such as Random Forest, Gradient Boosting, and Support Vector Regressor (SVR). All models were trained on the same feature set, using consistent training procedures, and evaluated on the real PPG test data using R-squared (R^2) and Root Mean Square Error (RMSE) as performance metrics.

As shown in Table 3, the EBM model achieved the highest R-squared (0.91) and the lowest RMSE (0.34), indicating the best performance in both explained variance and prediction error. This superior performance, coupled with its interpretability and robustness, indicates to us the selection of EBM as the preferred model for this study.

(a) PWV Distribution – Training Set

(b) PWV Distribution – Test Set
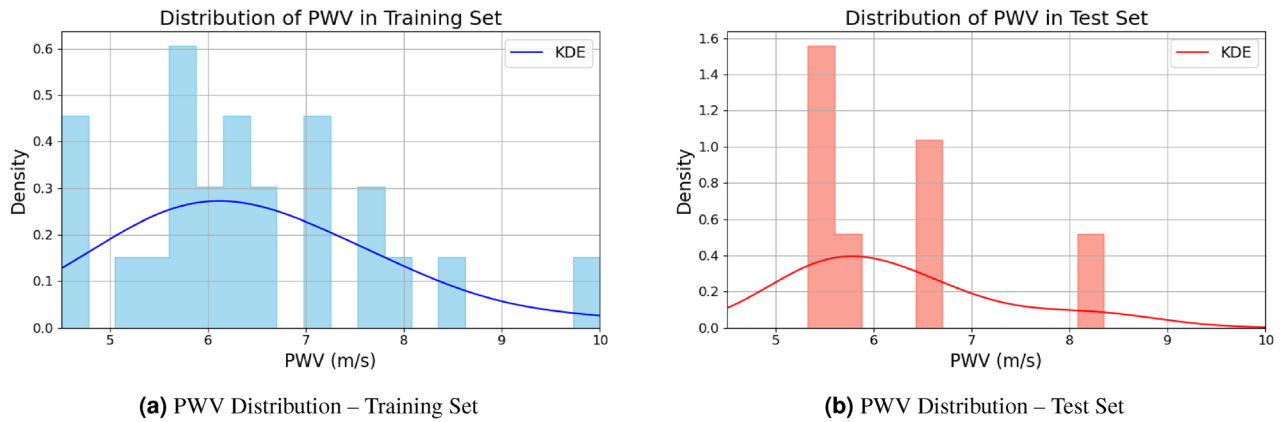
Fig. 7. Distribution of PWV values in the training and testing sets. The kernel density estimation (KDE) curves illustrate the spread and central tendency of both subsets. The training set (blue) and testing set (orange) cover a similar range, indicating a representative split of the data.

Hyperparameter	Search Range	Best Value
Learning Rate	[0.001, 1.0] (log-uniform)	0.0458
Max Bins	[32, 128]	96
Max Interaction Bins	[16, 64]	43
Max Leaves	[3, 7]	3
Min Samples per Leaf	[5, 20]	20

Table 4. Hyperparameter search space and optimal values obtained using TPE optimization.

Model training

To train the supervised machine learning models, the dataset was first divided into two separate subsets: 80% of the data was allocated to the training set, and the remaining 20% to the testing set. This split was performed randomly, with stratification where applicable, to preserve the distribution of the target variable and ensure a representative evaluation, as shown in Fig. 7. Both distributions span a comparable range, with a slightly higher frequency of values of PWV between 6 and 7 in the training set. These results confirm that the data split preserves the variability of the original dataset.

Prior to model training, all features were standardized using z-score normalization, transforming each feature to have a mean of 0 and a standard deviation of 1. This step was carried out using the statistics from the training set alone and then applied to the test set.

To enhance generalization and mitigate the risk of overfitting, we implemented 5-fold cross-validation within the training set. In this setup, the training data was further split into five folds: in each iteration, four folds were used to train the model, and the fifth fold was used for validation. The model's cross-validated performance was averaged across all folds, ensuring robust evaluation during the training phase. Additionally, to fine-tune the model's hyperparameters, we employed Bayesian optimization using the Tree-structured Parzen Estimator (TPE) algorithm provided by the Optuna library with the hyperparameter range defined as shown in Table 4 This method has demonstrated strong performance in optimizing complex models such as Explainable Boosting Machines (EBMs)[44,46,48,48]. Hyperparameter tuning was conducted within the cross-validation loop to avoid bias in performance estimation.

Model testing and evaluation

The EBM model's performance was evaluated using negative and positive testing strategies to assess its robustness and generalizability under diverse scenarios. For positive testing, the evaluation was conducted using two performance metrics: the R-squared (R^2) value and the root mean square error (RMSE), which measures the agreement between the actual and predicted values and its measure in m/s[20]. The R-squared value quantifies the proportion of variance in the dependent variable that is predictable from the independent variables. At the same time, the RMSE provides an estimate of the magnitude of prediction errors. These metrics were calculated as follows:

$$R^2 = 1 - \frac{\sum_{n=1}^{N}(PWV^n{\rm real} - PWV^n{\rm predicted})^2}{\sum_{n=1}^{N}(PWV^n{\rm real} - \mu(PWV{\rm real}))^2}, \tag{35}$$

$$\text{RMSE} = \sqrt{\frac{\sum_{n=1}^{N}(\text{PWV}^n\text{real} - \text{PWV}^n\text{predicted})^2}{N}}, \tag{36}$$

where μ is a function that evaluates the mean of PWV_{real} over the N subjects.

For negative testing, the RMSE metric was employed to assess the model's robustness under conditions where the target labels or data were randomized. In addition to the RMSE on the original test data, the median SEP was calculated across multiple permutations of the target labels to represent the typical error under the null hypothesis. The variability in these permuted RMSEs was assessed using the standard deviation of the RMSE across permutations. Finally, another key metric was the $Ratio_{Perm}$ metric, defined as the Ratio of the median SEP on permuted data to the SEP on original data, which was calculated as:

$$\text{Ratio}_{\text{P}}\text{erm} = \frac{\text{Median RMSE (Permuted Data)}}{\text{RMSE (Original Data)}}, \tag{37}$$

a higher $Ratio_{Perm}$ indicates a greater distinction between the model's performance on original and permuted datasets, highlighting its robustness and meaningful predictive capability.

These metrics were computed for positive and negative testing scenarios to ensure a comprehensive assessment of the EBM model's performance and ability to generalize under varying conditions. The combination of EBM's transparent framework, high predictive accuracy, and rigorous evaluation process highlights its effectiveness for this study.

Results and discussion

The primary aim of this study is to investigate the potential of using multiple weighted visibility graphs—extracted from multicycle PPG signals and their first and second derivatives—combined with image processing features for non-invasive PWV estimation. The results obtained from both in-silico and real PPG signals are compared with previous works that also estimate PWV using PPG-based methods.

In[21], PWV is estimated using a spectrogram as a signal-to-image transformation, with features based on energy, statistics, and the Schrödinger spectrum. In[49], a binary visibility graph is used with transfer learning for feature extraction. Furthermore,n[26], a limited penetrable weighted visibility graph, combines image-based features.

It is essential to note that, for real PPG signals, we did not compare our approach with the method proposed in[24], which is based on a deep learning model using CNNs and an attention mechanism. This is due to data limitations, as their method requires a larger dataset than what is available in our real-world recordings. Therefore, that comparison was performed only on the in-silico dataset.

The model's performance and robustness on the real dataset were evaluated using both traditional performance metrics and negative permutation testing. This dual evaluation aims to assess the model's predictive capabilities and generalization ability while minimizing the risk of overfitting. For the in-silico dataset, only standard (positive) testing was performed in this study.

In-silico data

Table 5 shows that the different algorithms presented a high performance for the in-silico dataset in the R^2 metric, showing the capacity of the models to capture information coming from the PPG signal to predict the PWV. In addition, this also shows the capacity of the proposed method to obtain a similar performance compared with the state-of-the-art techniques in the in-silico dataset. Furthermore, it can be seen that the proposed approach presented a lower *RMSE* value compared to the other methods, showing a more precise estimation of the PWV. However, to have a more realistic idea about the performance of the proposed models, it is necessary to test it in real PPG signals.

Real PPG data

Positive testing

Table 6 presents the performance of the models under positive testing, which involves evaluating the models on the test dataset. The proposed model outperforms the other two approaches, achieving an R^2 (coefficient of determination) of 0.91 and an RMSE of 0.34. These results highlight a noticeable drop in performance for the other models when applied to real PPG images, suggesting that the features effective for the in-silico dataset may not generalize well to real-world data.

Method	R-squared	RMSE (*m/s*)
Sprectrogram+DL[24]	0.99	0.21
Spectrogram+ML[21]	0.99	0.25
VG+DL[49]	0.99	0.19
VG+ML[26]	0.95	0.52
Ours	**0.99**	**0.16**

Table 5. Results obtained for the in-silico PPG dataset.

Method	R-squared	RMSE(m/s)
Spectrogram+ML[21]	0.34	1.12
VG+DL[49]	0.42	0.69
VG+ML[26]	0.81	0.39
Ours	**0.91**	**0.34**

Table 6. Results obtained for the real PPG dataset.
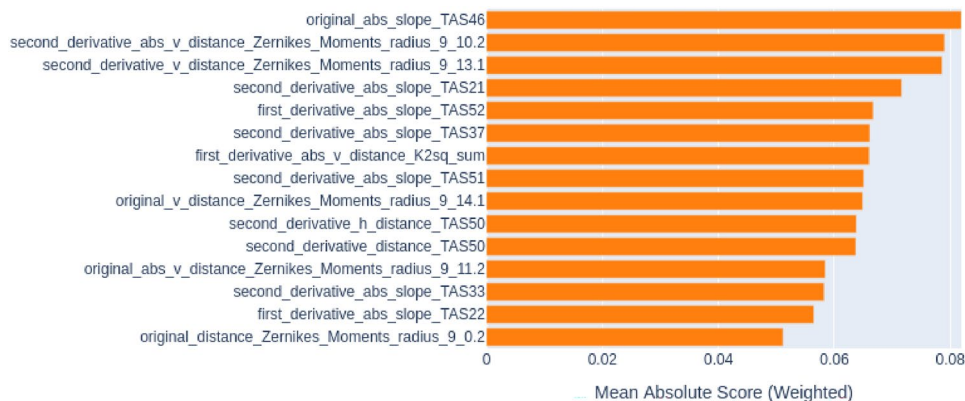
Fig. 8. Feature importance scores for the Explainable Boosting Machine (EBM) model applied to the real PPG dataset. The bar chart presents the top features contributing to the model's pulse wave velocity (PWV) estimation, ranked by their mean absolute (weighted) score. Notably, features derived from the second derivative of the PPG signal—particularly those based on TAS and Zernike moments. This highlights the relevance of capturing the PPG waveform's fine-grained temporal and morphological characteristics, with higher-order signal derivatives enhancing model performance through richer structural information.

In contrast, the proposed framework demonstrates a greater ability to capture relevant information related to PWV, outperforming the other approaches. Across all cases, models utilizing visibility graph-based representations consistently yielded better results than spectrograms. This underscores the potential of visibility graphs as an effective signal-to-image transformation method for PPG signals in PWV estimation.

Moreover, a key advantage of the visibility graph approach is its simplicity in image generation. Unlike spectrograms, which require careful parameter tuning, such as window type and length, the visibility graph does not depend on such signal-specific adjustments. This makes it more adaptable and suitable for real-time applications, as discussed in[21].

Furthermore, it is worth noting that among the methods using visibility graphs, the proposed approach and the method in[26] performed significantly better than the one presented in[49]. One key reason for this performance gap may be using a weighted visibility graph instead of the binary visibility graph used in[49]. While the binary VG captures only the connectivity between data points in the PPG signal, it fails to encode differences in the relationships between those points. In contrast, the weighted visibility graph enhances signal representation by incorporating quantitative information—depending on the chosen weighting rule—that reflects the nature of the connection between points. This enables a more nuanced description of the signal's morphology.(Fig. 8)

The use of multiple weighting schemes further enriches the image representation, capturing diverse aspects of the signal, such as time-based differences or horizontal distance between points. These enhancements contribute to more informative features for PWV estimation. Finally, our proposed method outperformed the one introduced in[26], demonstrating the added value of incorporating the first and second derivatives of the PPG signal. These derivatives provide additional insights into the velocity and acceleration of the signal, which are valuable for PWV prediction[19]. The Explainable Boosting Machine (EBM) model also contributed to this improvement, offering strong predictive performance and interoperability.

To further evaluate the performance of the proposed method, we generated scatter plots and Bland–Altman plots for both training and testing sets (Fig. 9). The scatter plot demonstrates a strong alignment between predicted and actual PWV values, with data points distributed closely around the ideal agreement line. This indicates good predictive capability across the proposed range of PWV values. Additionally, the Bland–Altman analysis further provides quantitative insights into the consistency of the predictions. In the training set, the mean bias was small (0.073), with acceptable limits of agreement (−0.30 to 0.45), suggesting that the model predicts PWV consistently within reasonable error margins. Similarly, in the testing set, the model exhibited a bias (−0.119) and agreement range (−0.63 to 0.39), indicating that predictions remained consistent when applied to unseen data. These results demonstrate a reliable predictive performance; it remains essential to validate these findings further in larger, independent cohorts to confirm the broader applicability and generalization of the model.

(a) Actual vs. Predicted cf-PWV   **(b)** Bland–Altman plot (Train set)   **(c)** Bland–Altman plot (Test set)
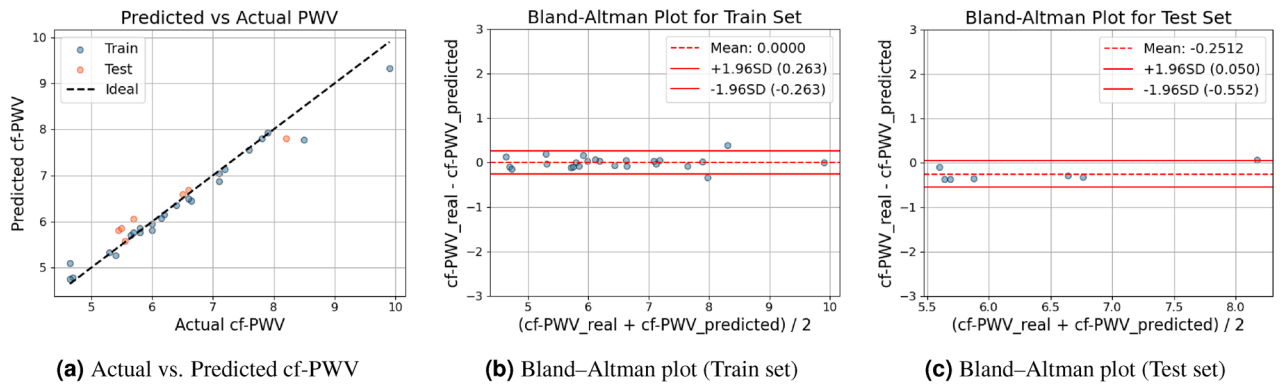
Fig. 9. Visual assessment of the EBM model's predictive performance. (**a**) Scatter plot comparing actual and predicted cf-PWV, showing good agreement. (**b**–**c**) Bland–Altman plots demonstrating prediction consistency and agreement for training and testing sets, respectively.

Metric	Values			
	Spectrogram+ML[21]	VG+DL[49]	VG+ML[26]	Ours
RMSE on original data	1.12	0.69	0.39	**0.34**
Median RMSE on permutation	1.72	0.73	0.94	**1.49**
SD of RMSE on permutation	0.17	0.18	0.16	**0.12**
Ratio_Perm	1.54	1.05	2.41	**4.38**
P_value	0.15	0.20	0.03	**0.01**

Table 7. Results of the permutation analysis of the real PPG dataset. The unit of measurement of RMSE are in m/s.

Additionally, one of the main advantages of the EBM model is the interpretability that this model provides (Fig.8) compared to other model ML models such as MLP. Figure 8 shows illustrates the relative importance of the 15 best features based on the different categories of features derived from the Explainable Boosting Machine (EBM) model for the PWV estimation. Morphological-based features, particularly Threshold Adjacency Statistics (TAS),shows a very promising performance having 9 of the 15 features. Features like $original\_abs\_slope\_TAS46$ and $second\_derivative\_abs\_slope\_TAS21$ ranked among the best features, shows the relevance to capture the variation on the local morphology of the visibility graph image representation. These morphological descriptors capture subtle waveform variations of the PPG that could be indicative of variations of arterial stiffness. This has been studied in the past[50,51], as variations in waveform morphology correlate strongly with changes in arterial compliance and vessel wall properties, which are well-established physiological determinants of pulse wave velocity. Shape-based features, particularly the ones obtained from Zernike's Moments, such as $second\_derivative\_abs\_v\_distance\_Zernikes\_Moments\ radius\_9\_10.2$ and $second\_derivative\_v\_distance\_Zernikes\_Moments\_radius\_9\_13.1$, also showed great predictive power. These shape-based metrics effectively encode geometric patterns and intricate structural details of the PPG waveform, providing robust complementary information that enhances prediction accuracy. Additionally, Semi-Classical Signal Analysis (SCSA)-based features, such as $first\_derivative\_abs\_v\_distance\_K2sq\_sum$, show the promising results of spectral and energy-related descriptors derived from eigenfunctions and eigenvalues of the Schrödinger operator. These features encapsulate complex spectral characteristics of the PPG signals, offering deeper insights into arterial properties not easily captured by traditional time-domain analyses. Finally, it is worth noting that most features displayed in Fig. 8 are derived from the visibility graphs obtained from the first and second derivatives, indicating that information about velocity and acceleration enhances the model's ability to estimate the PWV. This results in Concorde, which aligns with findings from the past[19], where it was demonstrated that information derived from derivatives can enhance model performance, given the physical interpretation of the phenomenon being estimated. Another interesting finding is that most of the relevant features belong to the TAS features, indicating that local morphology patterns from the visibility graph provide reliable information that allows the estimation of PWV.

Negative testing

To further assess the robustness of the model and ensure that its predictions are not the result of chance or noise, negative permutation testing was performed (Table 7). The RMSE of the proposed model on the original test data was 0.34, representing the best performance among all evaluated methods. This value was substantially lower than the median RMSE obtained from the permuted data, which was 1.49. This significant difference indicates

that the model performs considerably better on the original (correctly labeled) data than with randomized labels, thereby validating the model's predictive capabilities.

Additionally, the variability of the RMSE values across the permuted datasets, as indicated by the standard deviation (0.03), was relatively low. This consistency further reinforces the conclusion that the model's performance is not due to chance. If the model were capturing random noise, its performance would not significantly deteriorate when the labels are shuffled.

Moreover, the $Ratio_{Perm}$ metric—which quantifies the Ratio between the median RMSE on permuted data and the RMSE on the original test data—was calculated as 4.38. This high ratio demonstrates that the model's predictions on real data are more than four times more accurate than those on randomized data. These results provide strong evidence that the proposed model is capturing meaningful patterns in the data rather than overfitting to noise or spurious correlations and is, therefore, capable of generalizing to real-world scenarios.

Comparative analysis

To evaluate the effectiveness and robustness of the proposed framework, we conducted a comparative analysis against several state-of-the-art methods for pulse wave velocity (PWV) estimation. This evaluation included both positive testing on in-silico and real PPG datasets (Tables 5 and 6) and negative testing using permutation analysis (Table 7).

In the in-silico dataset (Table 5), all compared models achieved high R² values close to 0.99, reflecting the controlled nature of the simulated data. However, our proposed method obtained the lowest RMSE (0.16), indicating the most precise PWV estimation among the tested approaches. These results validate the effectiveness of our feature extraction strategy in ideal conditions. However, given the ideal conditions of the in-silico signal, it's important to test the performance of the proposed approach on real data, given a more realistic approximation of the performance of the proposed framework in a realistic scenario.

For the real PPG dataset (Table 6), the proposed method achieved an R² of 0.91 and RMSE of 0.34, outperforming other visibility graph–based methods (VG+DL [50], VG+ML [27]) and spectrogram-based approaches (Spectrogram+ML [22]), which exhibited significantly reduced accuracy compared to the performance on in-silico dataset. This demonstrates a great generalization ability of our framework in more realistic clinical scenarios.

Finally, to further validate the robustness of the proposed method, we performed negative testing via permutation analysis (Table 7). This approach evaluates model performance when the target variable (PWV) is randomly shuffled, ensuring that results are not due to chance. Our method showed a high RatioPerm value of 4.38, the highest among all compared methods, and a low p-value (0.01), indicating statistically significant performance above random. The RMSE on permuted data (1.49) was substantially higher than on the original data (0.34), confirming the model's ability to learn meaningful physiological patterns rather than overfitting to noise.

Together, these comparative results underscore the advantages of combining multi-weighted LPWVG representations with diverse feature modalities (shape, morphology, frequency, and energy). The proposed method is not only highly accurate under controlled conditions but also performs well in real data.

Generalizability and limitations

While the proposed LPWVG-based framework for PWV estimation demonstrates strong performance on both in-silico and real-world datasets, it is important to consider its generalizability and clinical contexts.

The model was trained and tested on a real PPG dataset consisting of 35 individuals aged 35–73, with PPG signals collected under controlled conditions. Although this dataset captures relevant physiological variability, it represents a relatively narrow demographic and PWV values. Additionally, it does not account for important clinical subgroups such as individuals with arrhythmias, diabetes, or peripheral vascular disease. Therefore, the model's performance in broader clinical populations, including patients with comorbidities or pediatric cases, remains to be validated.

Another limitation concerns the relatively small real-world dataset, which may limit the model's ability to fully capture population-level variability given the narrow values of PWV presented. Although we employed rigorous training strategies, including stratified group K-fold cross-validation, feature selection, and permutation-based validation, larger and more diverse datasets are essential to confirm the model's generalization capacity. Moreover, this study uses only single-site PPG recordings; future work will explore multi-modal approaches (e.g., ECG+PPG) to further enhance accuracy and clinical reliability.

Despite these limitations, the model's strong performance on real PPG data and its interpretability via the Explainable Boosting Machine (EBM) suggest promising potential for clinical translation. Future studies should aim to validate the framework on larger, multi-center datasets across different devices and patient populations, and assess its utility in continuous monitoring or disease-specific applications such as hypertension or vascular aging.

Conclusion and future work

In this study, we explored a novel data-driven framework for Pulse Wave Velocity (PWV) estimation using photoplethysmography (PPG) signals. Our results demonstrate the potential of PPG-based approaches to overcome limitations associated with traditional techniques, which often rely on the simultaneous acquisition of pulse waves at multiple arterial sites. This process is invasive, operator-dependent, and technically complex. In contrast, the proposed method leverages PPG's non-invasive, low-cost, and easily deployable nature, making it well-suited for broader clinical and remote healthcare applications.

Looking ahead, future research will focus on several key directions to strengthen the translational impact of this work. First, expanding the dataset to include a more extensive and diverse patient population is essential

to ensure the model's robustness across a wide range of cardiovascular profiles. Second, developing a real-time implementation optimizing the model for deployment on wearable or mobile platforms could facilitate continuous monitoring of arterial stiffness in everyday settings. Lastly, integrating multi-modal physiological signals may enhance prediction accuracy and improve the interpretability of model outputs, ultimately advancing the clinical utility of non-invasive PWV estimation tools.

Data availability
Data analyzed during the current study are available from the corresponding author on reasonable request.

References
1. Yusuf, S. et al. Modifiable risk factors, cardiovascular disease, and mortality in 155 722 individuals from 21 high-income, middle-income, and low-income countries (pure): a prospective cohort study. *The Lancet* **395**, 795–808 (2020).
2. Murray, C. J. et al. Global burden of 87 risk factors in 204 countries and territories, 1990–2019: a systematic analysis for the global burden of disease study 2019. *The lancet* **396**, 1223–1249 (2020).
3. Singh, G. M. et al. The age associations of blood pressure, cholesterol, and glucose: analysis of health examination surveys from international populations. *Circulation* **125**, 2204–2211 (2012).
4. Donato, A. J., Machin, D. R. & Lesniewski, L. A. Mechanisms of dysfunction in the aging vasculature and role in age-related disease. *Circ. research* **123**, 825–848 (2018).
5. Laurent, S. & Boutouyrie, P. Arterial stiffness and hypertension in the elderly. *Front. cardiovascular medicine* **7**, (2020).
6. Boutouyrie, P., Chowienczyk, P., Humphrey, J. D. & Mitchell, G. F. Arterial stiffness and cardiovascular risk in hypertension. *Circ. research* **128**, 864–886 (2021).
7. Tavallali, P., Razavi, M. & Pahlevan, N. M. Artificial intelligence estimation of carotid-femoral pulse wave velocity using carotid waveform. *Sci. reports* **8**, 1–12 (2018).
8. Marshall, A. G. et al. Update on the use of pulse wave velocity to measure age-related vascular changes. *Curr. hypertension* **26**, 131–140 (2024).
9. Ueda, I. et al. Comparability and reproducibility of the carotid-femoral pulse wave velocity measurements using a multi-element carotid tonometry sensor. *J. human hypertension* **22**, 699–703 (2008).
10. An, D.-W. et al. Derivation of an outcome-driven threshold for aortic pulse wave velocity: an individual-participant meta-analysis. *Hypertension* **80**, 1949–1959 (2023).
11. Bailey, M. A. et al. Carotid-femoral pulse wave velocity is negatively correlated with aortic diameter. *Hypertens. Res.* **37**, 926–932 (2014).
12. Azizzadeh, M. et al. Reference equations for pulse wave velocity, augmentation index, amplitude of forward and backward wave in a european general adult population. *Sci. Reports* **14**, 23151 (2024).
13. Laurent, S. et al. Expert consensus document on arterial stiffness: methodological issues and clinical applications. *Eur. heart journal* **27**, 2588–2605 (2006).
14. Yang, Y. et al. Assessment of aortic and peripheral arterial stiffness in patients with knee osteoarthritis by ultrasound doppler derived pulse wave velocity. *Sci. Reports* **14**, 1346 (2024).
15. for Arterial Stiffness' Collaboration, R. V. Determinants of pulse wave velocity in healthy people and in the presence of cardiovascular risk factors:'establishing normal and reference values'. *Eur. heart journal* **31**, 2338–2350 (2010).
16. Xu, L. et al. Improving the accuracy and robustness of carotid-femoral pulse wave velocity measurement using a simplified tube-load model. *Sci. Reports* **12**, 5147. https://doi.org/10.1038/s41598-022-09256-z (2022).
17. Park, S., Kwon, M., Nam, H. & Huh, H. Interpolation time-optimized aortic pulse wave velocity estimation by 4d flow mri. *Sci. Reports* **13**, 16484. https://doi.org/10.1038/s41598-023-43799-z (2023).
18. Pereira, T., Correia, C. & Cardoso, J. Novel methods for pulse wave velocity measurement. *J. medical biological engineering* **35**, 555–565 (2015).
19. Bahloul, M. A., Chahid, A. & Laleg-Kirati, T.-M. A multilayer perceptron-based carotid-to-femoral pulse wave velocity estimation using ppg signal. In *2021 IEEE EMBS International Conference on Biomedical and Health Informatics (BHI)*, 1–6 (IEEE, 2021).
20. Garcia, J. M. V., Bahloul, M. A. & Laleg-Kirati, T.-M. A multiple linear regression model for carotid-to-femoral pulse wave velocity estimation based on schrodinger spectrum characterization. In *2022 44th Annual International Conference of the IEEE Engineering in Medicine & Biology Society (EMBC)*, 143–147, https://doi.org/10.1109/EMBC48229.2022.9871031 (2022).
21. Vargas, J. M., Bahloul, M. A. & Laleg-Kirati, T.-M. A learning-based image processing approach for pulse wave velocity estimation using spectrogram from peripheral pulse wave signals: An in silico study. *Front. Physiol.* **14**, https://doi.org/10.3389/fphys.2023.1100570 (2023).
22. Vargas, J. M., Bahloul, M. A. & Laleg-Kirati, T. M. Ppg-based cf-pwv estimation using visibility graph image representation and transfer learning. In *2023 IEEE EMBS Special Topic Conference on Data Science and Engineering in Healthcare, Medicine and Biology*, 97–98, https://doi.org/10.1109/IEEECONF58974.2023.10405056 (2023).
23. Hellqvist, H., Karlsson, M., Hoffman, J., Kahan, T. & Spaak, J. Estimation of aortic stiffness by finger photoplethysmography using enhanced pulse wave analysis and machine learning. *Front. Cardiovasc. Medicine* **11**, https://doi.org/10.3389/fcvm.2024.1350726 (2024).
24. Pilevar Abrisham, K., Alipour, K., Tarvirdizadeh, B. & Ghamari, M. Advancing ppg-based cf-pwv estimation with an integrated cnn-bilstm-attention model. *Signal, Image and Video Process.* **18**, 8621–8633, https://doi.org/10.1007/s11760-024-03496-4 (2024).
25. Debuchy, V., Khalifa, M., Tresson, P., Thirion-Moreau, N. & Moreau, E. Machine learning techniques applied to in-silico pulse wave velocity estimation based on photoplethysmographic signals. In *2024 32nd European Signal Processing Conference (EUSIPCO)*, 1716–1720, https://doi.org/10.23919/EUSIPCO63174.2024.10715455 (2024).
26. Vargas, J. M., Boularas, M. M., Bahloul, M. A., Aridhi, S. & Laleg-Kirati, T. Pulse wave velocity estimation using photoplethysmogram-based limited penetrable weighted visibility graph features. *2024 46th Annu. Int. Conf. IEEE Eng. Medicine Biol. Soc. (EMBC)* 1–6 (2024).
27. Charlton, P. H. et al. Modeling arterial pulse waves in healthy aging: a database for in silico evaluation of hemodynamics and pulse wave indexes. *Am. J. Physiol. Circ. Physiol.* **317**, H1062–H1085 (2019).
28. Liang, Y., Elgendi, M., Chen, Z. & Ward, R. K. An optimal filter for short photoplethysmogram signals. *Sci. Data* **5** (2018).
29. The visibility graph. Lacasa, L., Luque, B., Ballesteros, F., Luque, J. & Nuñ o, J. C. From time series to complex networks. *Proc. Natl. Acad. Sci.* **105**, 4972–4975. https://doi.org/10.1073/pnas.0709247105 (2008).
30. Sannino, S., Stramaglia, S., Lacasa, L. & Marinazzo, D. Visibility graphs for fmri data: multiplex temporal graphs and their modulations across resting state networks. *bioRxiv* https://doi.org/10.1101/106443 (2017). arxiv:https://www.biorxiv.org/content/early/2017/04/03/106443.full.pdf.

31. Han, J. Analysis of gas-water flow transition characteristics based on multiscale limited penetrable visibility graph. *Sci. Reports* **10**, https://doi.org/10.1038/s41598-020-64021-4 (2020).
32. Sadoun, M. S. N. *et al.* Cognitive stress detection during physical activity using simultaneous, mobile eeg and ecg signals. *IFAC-PapersOnLine* **58**, 291–296, https://doi.org/10.1016/j.ifacol.2024.11.052 (2024). 12th IFAC Symposium on Biological and Medical Systems BMS 2024.
33. Nasrudin, M. W. et al. Moment invariants technique for image analysis and its applications: A review. *J. Physics: Conf. Ser.* **1962**, https://doi.org/10.1088/1742-6596/1962/1/012028 (2021).
34. Conseil, S., Bourennane, S. & Martin, L. Comparison of fourier descriptors and hu moments for hand posture recognition. In *2007 15th European Signal Processing Conference*, 1960–1964 (2007).
35. Huang, Z. & Leng, J. Analysis of hu's moment invariants on image scaling and rotation. In *2010 2nd International Conference on Computer Engineering and Technology*, vol. 7, V7–476–V7–480, https://doi.org/10.1109/ICCET.2010.5485542 (2010).
36. Li, S., Lee, M.-C. & Pun, C.-M. Complex zernike moments features for shape-based image retrieval. *IEEE Transactions on Syst. Man, Cybern. - Part A: Syst. Humans* **39**, 227–237. https://doi.org/10.1109/TSMCA.2008.2007988 (2009).
37. Hamilton, N., Pantelic, R., Hanson, K. & Teasdale, R. Fast automated cell phenotype classification. *BMC bioinformatics* **8**, 110. https://doi.org/10.1186/1471-2105-8-110 (2007).
38. Cho, B. H. *et al.* Fast micro calcication detection in ultrasound images using image enhancement and threshold adjacency statistics. *Proc. SPIE - The Int. Soc. for Opt. Eng.* **8670**, https://doi.org/10.1117/12.2007458 (2013).
39. Sanghavi, F., Kezebou, L., Panetta, K. & Agaian, S. Breast cancer classification using parametric free thresholding adjacency statistics based Fibonacci patterns. In Agaian, S. S., Asari, V. K., DelMarco, S. P. & Jassim, S. A. (eds.) *Mobile Multimedia/Image Processing, Security, and Applications 2020*, vol. 11399, 113990Q, https://doi.org/10.1117/12.2558613. International Society for Optics and Photonics (SPIE, 2020).
40. Mallat, S. & Zhong, S. Characterization of signals from multiscale edges. *IEEE Transactions on Pattern Analysis Mach. Intell.* **14**, 710–732. https://doi.org/10.1109/34.142909 (1992).
41. Laleg-Kirati, T.-M., Crépeau, E. & Sorine, M. Semi-classical signal analysis. *Math. Control. Signals, Syst.* **25**, 37–61 (2013).
42. Li, P. & Laleg-Kirati, T.-M. Central blood pressure estimation from distal ppg measurement using semiclassical signal analysis features. *IEEE Access* **9**, 44963–44973 (2021).
43. Laleg-Kirati, T. M., Crépeau, E. & Sorine, M. Semi-classical signal analysis. *Math. Control. Signals, Syst.* **25**, 37–61, https://doi.org/10.1007/s00498-012-0091-1 (2013). arxiv:1007.0938.
44. Arslan, A. K. & Colak, C. Explainable boosting machine approach to identifying risk factors for parkinson's disease. *Annals Med. Res.* **31**, 735–735 (2024).
45. Sarica, A., Quattrone, A. & Quattrone, A. Explainable boosting machine for predicting alzheimer's disease from mri hippocampal subfields. In Mahmud, M., Kaiser, M. S., Vassanelli, S., Dai, Q. & Zhong, N. (eds.) *Brain Informatics*, 341–350 (Springer International Publishing, Cham, 2021).
46. Elgeldawi, E., Sayed, A., Galal, A. R. & Zaki, A. M. Hyperparameter tuning for machine learning algorithms used for arabic sentiment analysis. *Informatics* **8**, https://doi.org/10.3390/informatics8040079 (2021).
47. Thimoteo, L. M. et al. Explainable artificial intelligence for covid-19 diagnosis through blood test variables. *J. Control. Autom. Electr. Syst.* **33**, 625–644 (2022).
48. Khattak, A., Zhang, J., Chan, P.-W., Chen, F. & Matara, C. M. Ai-supported estimation of safety critical wind shear-induced aircraft go-around events utilizing pilot reports. *Heliyon* **10** (2024).
49. Vargas, J. M., Bahloul, M. A. & Laleg-Kirati, T.-M. Ppg-based cf-pwv estimation using visibility graph image representation and transfer learning. In *2023 IEEE EMBS Special Topic Conference on Data Science and Engineering in Healthcare, Medicine and Biology*, 97–98, https://doi.org/10.1109/IEEECONF58974.2023.10405056 (2023).
50. Nichols, W. W., O'Rourke, M. F. & Vlachopoulos, C. *McDonald's Blood Flow in Arteries: Theoretical, Experimental and Clinical Principles* (CRC Press, 2011), 6th edn.
51. Townsend, R. R. et al. Recommendations for improving and standardizing vascular research on arterial stiffness. *Hypertension* **66**, 698–722. https://doi.org/10.1161/HYPERTENSIONAHA.115.06354 (2015).

Author contributions

The authors confirm their contribution to the paper as follows: Study conception, design, and implementation: All the authors contributed to the analysis and interpretation of results. All authors reviewed the results and approved the final version of the manuscript.

Declarations

Competing interests
The authors declare no conflict of interest.

Additional information
Correspondence and requests for materials should be addressed to T.-M.L.-K.

Reprints and permissions information is available at www.nature.com/reprints.

Publisher's note Springer Nature remains neutral with regard to jurisdictional claims in published maps and institutional affiliations.